AIAA JOURNAL
Vol. 47, No. 4, April 2009

Accuracy of Bhatnagaar–Gross–Krook Scheme in Solving Laminar Viscous Flow Problems

Ashraf A. Omar,* Ong J. Chit,† Waqar Asrar,‡ and Ahmad F. Ismail§
International Islamic University Malaysia, Kuala Lumpur 50728, Malaysia

DOI: 10.2514/1.35247

This paper describes the development of a gas-kinetic solver to compute laminar viscous flows in two-space dimensions via a finite difference approach. The convection flux terms of the Navier–Stokes equations are discretized by a semidiscrete finite difference method. The resulting inviscid flux function is then determined by a numerical scheme that is based on the Bhatnagaar–Gross–Krook model of the approximate collisional Boltzmann equation. The scheme is based on the direct splitting of the inviscid flux function with inclusion of particle collisions in the transport process. As for the diffusion flux terms, they are discretized by a second-order central difference scheme. The cell interface values required by the gas-kinetic scheme are reconstructed to higher-order spatial accuracy via the monotone upstream-centered schemes for conservation laws variable interpolation method. An explicit-type time integration method known as the modified fourth-order Runge–Kutta is employed for computing steady-state solutions. In the numerical case studies, the results obtained from the flux vector splitting Bhatnagaar–Gross–Krook scheme are compared with available experimental data, analytical solutions, the results from upwind schemes, and the results from central difference scheme to verify the accuracy and robustness of the gas-kinetic solver. The tests have shown that the Bhatnagaar–Gross–Krook scheme is able to resolve the shear layer, the shock structure, and the flow accurately as the results compare favorably with the available experimental and analytical data.

Nomenclature

C_p	=	pressure coefficient
F, G	=	inviscid flux vector in Cartesian coordinates
$\bar{F}, \bar{G}$	=	inviscid flux vector in generalized coordinates
F_v, G_v	=	viscous flux vector in Cartesian coordinates
$\bar{F}_v, \bar{G}_v$	=	viscous flux vector in generalized coordinates
i, j	=	grid point location
M_∞	=	freestream Mach number
n	=	time level
Pr	=	Prandtl number
Re_∞	=	freestream Reynolds number
t	=	time
W	=	conservative variable in Cartesian coordinates
$\bar{W}$	=	conservative variable in generalized coordinates
γ	=	specific heat ratio
$\Delta\xi, \Delta\eta$	=	spatial step in generalized coordinates
θ	=	angle

I. Introduction

THROUGHOUT the history of computational fluid dynamics development, many numerical schemes have been created to solve practical application of gas dynamics problems. The key design criterion of any numerical scheme is to maximize robustness and accuracy. This requirement is particularly important in full Navier–Stokes solutions involving high-speed flow where intense shock waves and boundary layers may simultaneously exist. Among those notable and successful are the Godunov-type and flux vector splitting schemes. Besides these numerical schemes that stem from the discretization of the Euler equations, the gas-kinetic schemes have attracted much attention in recent years due to their high robustness and accuracy in solving compressible flow problems.

In the family of Godunov-type schemes, the Roe FDS (flux difference splitting) scheme [1] is the most popular, owing to its accuracy for compressible flow computations. However, the occurrence of transverse shock instability and negative internal energy, which are inherent of Godunov-type schemes, hinder their usage in the computation of high-speed flows with strong shock waves and expansion fans [2]. This is supported by the findings of Peery and Imlay [3] for blunt body computations with the Roe FDS scheme, which produce carbuncle phenomenon. In addition to FDS schemes, another group of schemes that belongs to the family of upwind schemes is flux vector splitting (FVS). FVS schemes such as Steger and Warming's [4] and Van Leer's [5] are known to be simple and robust in the capture of intense shocks and rarefaction waves. It is well known that FVS schemes have a large numerical dissipation on contact discontinuities, which explains the reason for their poor shock resolution capability at contact discontinuities [6].

Recent developments have seen the emergence of another class of scheme known as the gas-kinetic schemes that are developed based on the Boltzmann equation [7,8]. Mainly, there are two groups of gas-kinetic schemes, and the difference lies within the type of Boltzmann equation use in the gas evolution stage. One of them is the well-known KFVS (kinetic flux vector splitting) scheme which is based on the collisionless Boltzmann equation and the other is based on the collisional BGK (Bhatnagaar–Gross–Krook) model [9] where the BGK scheme is derived. Like any other FVS method, the KFVS scheme is very diffusive and less accurate in comparison with the Roe-type FDS method. The diffusivity of the FVS schemes is mainly due to the particle or wave-free transport mechanism, which sets the CFL time step equal to particle collision time [10]. To reduce diffusivity, particle collisions have to be modeled and implemented into the gas evolution stage. One of the distinct approaches to take particle collision into consideration in gas evolution can be found in Xu [7]. In this method, the collision effect is considered by the BGK model as an approximation of the collision integral in the Boltzmann equation. It is found that this gas-kinetic BGK scheme possesses accuracy that is superior to the flux vector splitting schemes and avoids the anomalies of FDS-type schemes [2,11–14].

Most of the developments of the gas-kinetic schemes are focused on solving fluid governing equations or flow problems via the finite

Presented as Paper 751 at the 46th AIAA Aerospace Sciences Meeting and Exhibit, Grand Sierra Resort Hotel, Reno, NV, 7–10 January 2008; received 22 October 2007; revision received 19 September 2008; accepted for publication 18 December 2008.

*Professor, Department of Mechanical Engineering, Member AIAA.
†Research Assistant, Department of Mechanical Engineering.
‡Professor, Department of Mechanical Engineering.
§Professor, Department of Mechanical Engineering.

volume method. May et al. [15] have applied the gas-kinetic BGK finite volume method for computing three-dimensional transonic flow with unstructured mesh. Zhang et al. [16] have developed a second-order KFVS scheme for shallow water flows in one-dimension space using the finite volume method. Xu et al. [17] used the BGK scheme cast in a finite volume manner to study complicated flow phenomena that occur in a laminar hypersonic viscous flows, that is, shock boundary layer interaction, flow separation, and viscous/inviscid interaction. These are just a few of the many applications of the gas-kinetic schemes in the finite volume framework. On the other hand, only a limited number of efforts are channeled into the development of the gas-kinetic schemes via the finite difference method. To name a few, Ravichandran [18] in 1997 developed higher-order KFVS algorithms using compact upwind difference operators to compute two-dimensional compressible Euler equations, and Ong et al. [13] in 2006 successfully extended the BGK scheme to solve compressible inviscid hypersonic flow problems.

In this paper, a flux vector splitting BGK scheme is developed to solve Navier–Stokes equations using the finite difference method. In this gas-kinetic scheme, the convective flux functions are approximated by the BGK model, which is based on the collisional Boltzmann equation. Four numerical test cases are presented here to investigate the accuracy and robustness of the developed solver, namely, flow passed a 7.5 deg compression corner, laminar flow passed a flat plate, hypersonic flow passed a 24 deg compression ramp, and hypersonic flow around a blunt body. The computed results are verified by comparing them with available experimental data, analytical solutions, the results from upwind schemes, and the results from central difference schemes.

II. Governing Equations

The two-dimensional normalized compressible Navier–Stokes equations can be written in the strong conservative form as

$$\frac{\partial W}{\partial t}+\frac{\partial F}{\partial x}+\frac{\partial G}{\partial y}=\frac{\partial F_v}{\partial x}+\frac{\partial G_v}{\partial y} \tag{1}$$

Where

$$W=\begin{bmatrix}\rho\\ \rho U\\ \rho V\\ \rho\varepsilon\end{bmatrix},\qquad F=\begin{bmatrix}\rho U\\ \rho U^2+p\\ \rho UV\\ (\rho\varepsilon+p)U\end{bmatrix},\qquad G=\begin{bmatrix}\rho V\\ \rho UV\\ \rho V^2+p\\ (\rho\varepsilon+p)V\end{bmatrix}$$

$$F_v=\begin{bmatrix}0\\ \tau_{xx}\\ \tau_{xy}\\ U\tau_{xx}+V\tau_{xy}-q_x\end{bmatrix},\qquad G_v=\begin{bmatrix}0\\ \tau_{xy}\\ \tau_{yy}\\ U\tau_{xy}+V\tau_{yy}-q_y\end{bmatrix}$$

$$\tau_{xx}=\frac{\mu}{Re_\infty}\left(\frac{4}{3}\frac{\partial U}{\partial x}-\frac{2}{3}\frac{\partial V}{\partial y}\right),\qquad \tau_{yy}=\frac{\mu}{Re_\infty}\left(\frac{4}{3}\frac{\partial V}{\partial y}-\frac{2}{3}\frac{\partial U}{\partial x}\right)$$

$$\tau_{xy}=\frac{\mu}{Re_\infty}\left(\frac{\partial U}{\partial y}+\frac{\partial V}{\partial x}\right),\qquad q_x=-\frac{\mu}{Re_\infty Pr(\gamma-1)M_\infty^2}\frac{\partial T}{\partial x}$$

$$q_y=-\frac{\mu}{Re_\infty Pr(\gamma-1)M_\infty^2}\frac{\partial T}{\partial y}$$

where ρ, U, V, p, ε, and T are the macroscopic density, x-component of velocity, y-component of velocity, pressure, total energy, and temperature, respectively. In addition, τ_{xx}, τ_{xy}, and τ_{yy} are the shear stress terms, and q_x and q_y are the heat conduction terms. The term μ is the dynamic viscosity of the viscous flow and is calculated via Sutherland's law. The normalization has been carried out by using the following freestream reference quantities: density ρ_∞, velocity U_∞, pressure $\rho_\infty U_\infty^2$, temperature T_∞, reference length L_∞, and reference time L_∞/U_∞.

To employ the preceding governing equations for a finite difference application, a transformation from the Cartesian coordinates (x, y) to generalized coordinates (ξ, η) is necessary. The resulting transformation yields the following form:

$$\frac{\partial \bar{W}}{\partial t}+\frac{\partial \bar{F}}{\partial \xi}+\frac{\partial \bar{G}}{\partial \eta}=\frac{\partial \bar{F}_v}{\partial \xi}+\frac{\partial \bar{G}_v}{\partial \eta} \tag{2}$$

where

$$\bar{W}=W/J,\qquad \bar{F}=(\xi_x F+\xi_y G)/J,\qquad \bar{G}=(\eta_x F+\eta_y G)/J$$
$$\bar{F}_v=(\xi_x F_v+\xi_y G_v)/J,\qquad \bar{G}_v=(\eta_x F_v+\eta_y G_v)/J$$

The metric terms that appear in the preceding equations are related to the derivatives of x and y by

$$\xi_x=Jy_\eta,\qquad \xi_y=-Jx_\eta,\qquad \eta_x=-Jy_\xi,\qquad \eta_y=Jx_\xi \tag{3}$$

and the Jacobian of transformation is given by

$$J=1/(x_\xi y_\eta-y_\xi x_\eta) \tag{4}$$

The manner in which these terms are evaluated is clearly described by Hoffmann and Chiang [19].

III. Numerical Methods

The present work is an extension of the inviscid flow solver developed in the previous studies [12,13] to incorporate diffusion terms into the solver to facilitate the simulation of viscous flow. Realizing this fact, the formulations of the BGK scheme to approximate the flux functions of the convective terms found in the compressible Navier–Stokes equations would remain totally the same as the previous studies, thus, without any due elaboration on the aspects of the development of the BGK scheme. The convective flux function $\bar{F}$ at a given cell interface, expressed in generalized coordinates, can be written as follows:

$$\bar{F}_{i+1/2,j}=(1-\phi)\bar{F}^e_{i+1/2,j}+\phi\bar{F}^f_{i+1/2,j} \tag{5}$$

where ϕ is an adaptive parameter and the superscripts e and f correspond to equilibrium and freestream flux functions, respectively. As for the numerical inviscid flux function at the cell interface in the η direction, it is obtained in a similar manner and presented as

$$\bar{G}_{i,j+1/2}=(1-\varphi)\bar{G}^e_{i,j+1/2}+\varphi\bar{G}^f_{i,j+1/2} \tag{6}$$

The necessary treatment and formulations required to calculate the equilibrium and freestream flux functions appearing in both Eqs. (5) and (6) are explained in detail in the previous works, and they can be found in [12,13].

In extending the numerical schemes (i.e., BGK, the Roe FDS, and the Steger–Warming FVS) to high-order spatial accuracy, the monotone upstream-centered schemes for conservation laws) approach [6] is adopted together with the min-mod limiter. Hence, the left and right states of the primitive variables ρ, U, V, and p at a cell interface could be obtained through the nonlinear reconstruction of the respective variables and are given as

$$\begin{aligned}Q_l&=Q_{i,j}+\frac{1}{2}\sigma\left(\frac{\Delta Q_{i+1/2,j}}{\Delta Q_{i-1/2,j}}\right)\Delta Q_{i-1/2,j},\\ Q_r&=Q_{i+1,j}-\frac{1}{2}\sigma\left(\frac{\Delta Q_{i+3/2,j}}{\Delta Q_{i+1/2,j}}\right)\Delta Q_{i+1/2,j}\end{aligned} \tag{7}$$

where Q is any primitive variables and the subscripts l and r correspond to the left- and right-hand side of a considered cell interface. In addition, $\Delta Q_{i+1/2,j}=Q_{i+1,j}-Q_{i,j}$. The min-mod limiter σ used in the reconstruction of flow variables in Eq. (7) is given as

$$\sigma(\Omega)=\min-\mathrm{mod}(1,\Omega)=\max[0,\min(1,\Omega)] \tag{8}$$

where the term Ω represents the ratio inside the parentheses of Eq. (7).

The diffusion flux terms that appear in the transformed Navier–Stokes equations of Eq. (2) are expressed in terms of shear stresses in Cartesian coordinates. Upon substitution of the relevant transformed shear stresses into the viscous flux vectors, the following form is obtained [19]:

$$\bar{F}_v = \frac{\mu}{Re_\infty J}\begin{bmatrix} 0 \\ (\frac{4}{3}\xi_x^2+\xi_y^2)U_\xi + (\frac{1}{3}\xi_x\xi_y)V_\xi + (\frac{4}{3}\xi_x\eta_x+\xi_y\eta_y)U_\eta + (\xi_y\eta_x-\frac{2}{3}\xi_x\eta_y)V_\eta \\ (\frac{1}{3}\xi_x\xi_y)U_\xi + (\xi_x^2+\frac{4}{3}\xi_y^2)V_\xi + (\xi_x\eta_y-\frac{2}{3}\xi_y\eta_x)U_\eta + (\xi_x\eta_x+\frac{4}{3}\xi_y\eta_y)V_\eta \\ \frac{1}{2}(\frac{4}{3}\xi_x^2+\xi_y^2)(U^2)_\xi + \frac{1}{2}(\xi_x^2+\frac{4}{3}\xi_y^2)(V^2)_\xi + (\frac{1}{3}\xi_x\xi_y)(UV)_\xi + \frac{1}{Pr(\gamma-1)M_\infty^2}(\xi_x^2+\xi_y^2)T_\xi \\ +\frac{1}{2}(\frac{4}{3}\xi_x\eta_x+\xi_y\eta_y)(U^2)_\eta + \frac{1}{2}(\xi_x\eta_x+\frac{4}{3}\xi_y\eta_y)(V^2)_\eta + (\xi_y\eta_x-\frac{2}{3}\xi_x\eta_y)UV_\eta \\ +(\xi_x\eta_y-\frac{2}{3}\xi_y\eta_x)VU_\eta + \frac{1}{Pr(\gamma-1)M_\infty^2}(\xi_x\eta_x+\xi_y\eta_y)T_\eta \end{bmatrix} \tag{9}$$

$$\bar{G}_v = \frac{\mu}{Re_\infty J}\begin{bmatrix} 0 \\ (\frac{4}{3}\xi_x\eta_x+\xi_y\eta_y)U_\xi + (\xi_x\eta_y-\frac{2}{3}\xi_y\eta_x)V_\xi + (\frac{4}{3}\eta_x^2+\eta_y^2)U_\eta + (\frac{1}{3}\eta_x\eta_y)V_\eta \\ (\xi_y\eta_x-\frac{2}{3}\xi_x\eta_y)U_\xi + (\xi_x\eta_x+\frac{4}{3}\xi_y\eta_y)V_\xi + (\frac{1}{3}\eta_x\eta_y)U_\eta + (\eta_x^2+\frac{4}{3}\eta_y^2)V_\eta \\ \frac{1}{2}(\frac{4}{3}\eta_x^2+\eta_y^2)(U^2)_\eta + \frac{1}{2}(\eta_x^2+\frac{4}{3}\eta_y^2)(V^2)_\eta + (\frac{1}{3}\eta_x\eta_y)(UV)_\eta + \frac{1}{Pr(\gamma-1)M_\infty^2}(\eta_x^2+\eta_y^2)T_\eta \\ +\frac{1}{2}(\frac{4}{3}\xi_x\eta_x+\xi_y\eta_y)(U^2)_\xi + \frac{1}{2}(\xi_x\eta_x+\frac{4}{3}\xi_y\eta_y)(V^2)_\xi + (\xi_y\eta_x-\frac{2}{3}\xi_x\eta_y)VU_\xi \\ +(\xi_x\eta_y-\frac{2}{3}\xi_y\eta_x)UV_\xi + \frac{1}{Pr(\gamma-1)M_\infty^2}(\xi_x\eta_x+\xi_y\eta_y)T_\xi \end{bmatrix} \tag{10}$$

The results presented previously provide the necessary viscous flux vectors needed for the discretization of the diffusion term $(\partial\bar{F}_v/\partial\xi + \partial\bar{G}_v/\partial\eta)$ in generalized coordinates. For the current work, a second-order central difference scheme is adopted for the approximation of the diffusion term. All the terms inside the viscous flux vectors can be defined as a product in the following general form:

$$(N)(M_k) \tag{11}$$

where the subscript k can either be ξ or η, depending on the term considered inside viscous flux vector. The terms N and M, where for example, the first term of the second component of viscous flux vector $\bar{F}_v$ would take the following expressions:

$$N = \frac{\mu}{Re_\infty J}\left(\frac{4}{3}\xi_x^2+\xi_y^2\right) \quad \text{and} \quad M = U \tag{12}$$

Hence, using this general formulation, the second-order central difference approximation for the considered term can be written as

$$\begin{aligned}\left(\frac{\partial\bar{F}_v}{\partial\xi}\right)_{1^{st}\text{term},2^{nd}\text{component}} &= \frac{\partial}{\partial\xi}(LM_\xi) \\ &= \frac{(LM_\xi)_{i+1/2,j}-(LM_\xi)_{i-1/2,j}}{\Delta\xi} \\ &= \frac{L_{i+1/2,j}(\frac{M_{i+1,j}-M_{i,j}}{\Delta\xi}) - L_{i-1/2,j}(\frac{M_{i,j}-M_{i-1,j}}{\Delta\xi})}{\Delta\xi} \\ &= \frac{L_{i+1/2,j}(M_{i+1,j}-M_{i,j}) - L_{i-1/2,j}(M_{i,j}-M_{i-1,j})}{(\Delta\xi)^2}\end{aligned} \tag{13}$$

The term located at the cell interface found in Eq. (13) is computed through the method of averaging between two neighboring points. Thus, by adopting and expanding the procedure to other terms found in the viscous flux vectors as outlined beforehand, the second-order central difference approximation of the diffusion term can be easily implemented. This manner of treating the diffusion term is employed for all the numerical schemes studied in this paper.

As for the time integration for steady-state problems, an explicit formulation is chosen for the current solver which uses a fourth-order Runge–Kutta method. Applying this method to the generalized two-dimensional Navier–Stokes equations provides the following result:

$$\begin{aligned}\bar{W}_{i,j}^{(1)} &= \bar{W}_{i,j}^n \\ \bar{W}_{i,j}^{(2)} &= \bar{W}_{i,j}^n - \frac{\Delta t}{4}\left[\left(\frac{\partial\bar{F}}{\partial\xi}\right)_{i,j}^{(1)} + \left(\frac{\partial\bar{G}}{\partial\eta}\right)_{i,j}^{(1)} - \left(\frac{\partial\bar{F}_v}{\partial\xi}\right)_{i,j}^{(1)} - \left(\frac{\partial\bar{G}_v}{\partial\eta}\right)_{i,j}^{(1)}\right] \\ \bar{W}_{i,j}^{(3)} &= \bar{W}_{i,j}^n - \frac{\Delta t}{3}\left[\left(\frac{\partial\bar{F}}{\partial\xi}\right)_{i,j}^{(2)} + \left(\frac{\partial\bar{G}}{\partial\eta}\right)_{i,j}^{(2)} - \left(\frac{\partial\bar{F}_v}{\partial\xi}\right)_{i,j}^{(2)} - \left(\frac{\partial\bar{G}_v}{\partial\eta}\right)_{i,j}^{(2)}\right] \\ \bar{W}_{i,j}^{(4)} &= \bar{W}_{i,j}^n - \frac{\Delta t}{2}\left[\left(\frac{\partial\bar{F}}{\partial\xi}\right)_{i,j}^{(3)} + \left(\frac{\partial\bar{G}}{\partial\eta}\right)_{i,j}^{(3)} - \left(\frac{\partial\bar{F}_v}{\partial\xi}\right)_{i,j}^{(3)} - \left(\frac{\partial\bar{G}_v}{\partial\eta}\right)_{i,j}^{(3)}\right] \\ \bar{W}_{i,j}^{n+1} &= \bar{W}_{i,j}^n - \Delta t\left[\left(\frac{\partial\bar{F}}{\partial\xi}\right)_{i,j}^{(4)} + \left(\frac{\partial\bar{G}}{\partial\eta}\right)_{i,j}^{(4)} - \left(\frac{\partial\bar{F}_v}{\partial\xi}\right)_{i,j}^{(4)} - \left(\frac{\partial\bar{G}_v}{\partial\eta}\right)_{i,j}^{(4)}\right]\end{aligned} \tag{14}$$

To save computing time; the viscous fluxes are only computed at the first stage of the Runge–Kutta scheme and frozen for the remaining stages [20,21].

In this paper, the computed numerical solutions of the BGK scheme for these test cases are compared with available experimental data, exact solutions, and results from other numerical schemes such as the Roe FDS, Steger–Warming FVS, and central difference scheme with TVD. Hence, in order to provide a more realistic and reasonable comparison among the numerical schemes stated in this paper, the development of the flow solvers for the BGK, the Roe FDS, and the Steger–Warming FVS schemes is based on the same

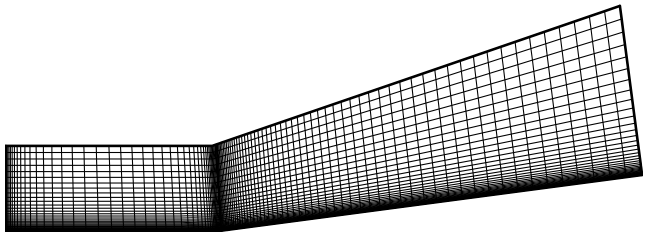

Fig. 1 Computational domain for the 7.5 deg compression corner.

Level	P (Pa)
18	3200.00
17	3058.82
16	2917.65
15	2776.47
14	2635.29
13	2494.12
12	2352.94
11	2211.76
10	2070.59
9	1929.41
8	1788.24
7	1647.06
6	1505.88
5	1364.71
4	1223.53
3	1082.35
2	941.18
1	800.00

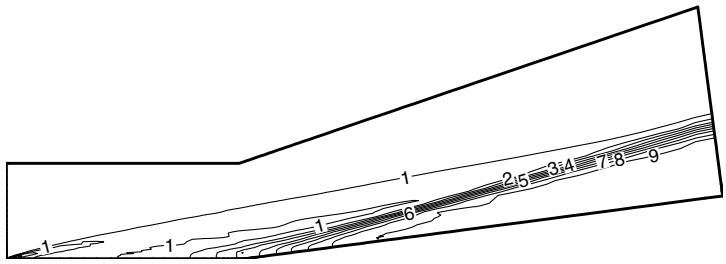

Fig. 2 Pressure contours for the 7.5 deg compression corner by BGK scheme.

founding basis where the same discretization method is used for the convective term, diffusion term, and temporal term. As for the discretization of the convective term, a semidiscrete finite difference scheme is used and presented as

$$\frac{\partial \bar{F}}{\partial \xi} + \frac{\partial \bar{G}}{\partial \eta} = \frac{\bar{F}_{i+1/2,j} - \bar{F}_{i-1/2,j}}{\Delta \xi} + \frac{\bar{G}_{i,j+1/2} - \bar{G}_{i,j-1/2}}{\Delta \eta} \tag{15}$$

The resulting inviscid flux functions at the cell interface are then approximated by the corresponding numerical schemes such as BGK, the Roe FDS, or the Steger–Warming FVS. The details relating to the treatment of the inviscid flux functions by the Roe FDS and the Steger–Warming FVS are readily available from past published works such as [1,4,6,19], respectively. Although the discretization method for the central difference scheme would differ from the scheme stated in Eq. (15), instead the following procedure is used:

$$\frac{\partial \bar{F}}{\partial \xi} + \frac{\partial \bar{G}}{\partial \eta} = \frac{\bar{F}_{i+1,j} - \bar{F}_{i-1,j}}{2\Delta \xi} + \frac{\bar{G}_{i,j+1} - \bar{G}_{i,j-1}}{2\Delta \eta} \tag{16}$$

It is a well-known fact that the determination of the inviscid flux functions by the central difference scheme in such a manner would produce unwanted oscillations in the solutions; the remedy is to include the addition of damping terms or TVD into the solver, and a detailed explanation about this matter can be found in [6,19].

IV. Results and Discussions

A. 7.5 Degree Compression Corner

This test problem is intended to demonstrate the accuracy and robustness of the BGK scheme developed in this study over the conventional Godunov-type numerical schemes, namely the Roe FDS and the Steger–Warming FVS schemes at a high Mach number. In addition, the experimental data quoted by Simeonides et al. [22] are also used to validate the computed results of the present schemes.

The mesh size used for this problem is 100×50 grid points, which are clustered in the transverse direction and at a location close to the corner in the streamwise direction. The flow geometry and grid are shown in Fig. 1. The freestream conditions are as follows: Mach number $M_\infty = 6.0$, density $\rho_\infty = 0.04142\ \text{kg/m}^3$, temperature $T_\infty = 57.3$ K, and Reynolds number $Re_\infty = 8 \times 10^5$. The Reynolds number is based on a reference length taken as $L_\infty = 0.08$ m. At the left boundary of the computational domain, inflow conditions are specified as freestream conditions. As for the right and top boundaries, their conditions are determined by means of extrapolation from the interior domain. The bottom boundary that places the compression corner is set to assume no-slip boundary conditions. The computation is impulsively started and marched to steady state.

The computed flowfield of this flow problem depicting the pressure contours that are produced by the BGK scheme is shown in Fig. 2. In addition, other computed results such as surface pressure coefficient and skin friction coefficient are presented in Fig. 3 and 4, respectively. Through these figures, comparisons are made among the numerical schemes themselves and to the experimental data that will provide a good ground to assess the computational behaviors of each scheme. The circle symbol in black in these figures represents the experimental data. As shown in Fig. 3, the BGK scheme is able to give computed results that agree best with the experimental data if compared with the Roe FDS and Steger–Warming FVS schemes' results. Similarly, the results depicted by Fig. 4 also point to the same conclusion. The computed results produced by the Steger–Warming FVS scheme, which are shown via Fig. 3 and 4, are poor and inaccurate. This is due to the fact that the diffusion error in the Steger–Warming FVS scheme is high and can not be cured with high-order spatial approximation methods. Observations made through these figures clearly show that the BGK scheme is better when compared with the Roe FDS and the Steger–Warming schemes in terms of accuracy.

B. Laminar Flow Passed a Flat Plate

In this test problem, a boundary layer on a flat plate is calculated. The development of the boundary layer on this flat plate provides a good opportunity to asses the accuracy of the numerical schemes for incompressible flow problems because an exact solution of Blasius [23] is available for comparison with the computed results.

The problem's geometry is a rectangular domain with a grid size of 241×81 points uniformly distributed in both directions as shown in

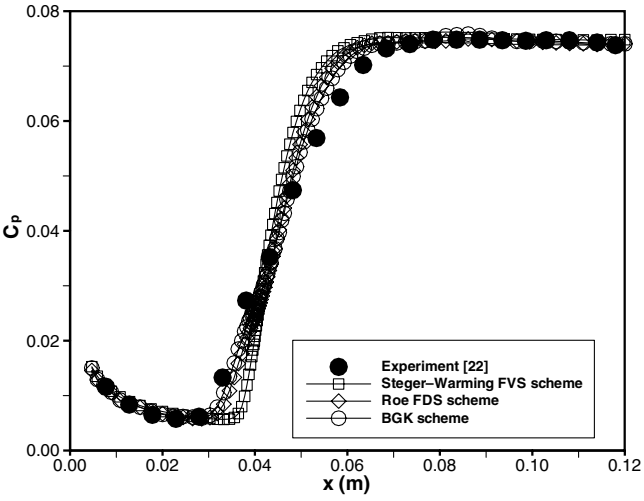

Fig. 3 Surface pressure coefficients for the 7.5 deg compression corner.

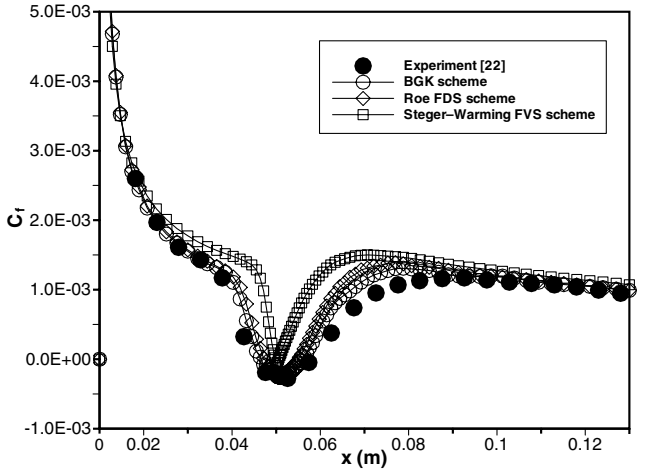

Fig. 4 Surface skin friction coefficients for the 7.5 deg compression corner.

Fig. 5. The computation is implemented with the following flow conditions: Mach number $M_\infty = 0.2$, density $\rho_\infty = 0.00283$ kg/m^3, temperature $T_\infty = 388.9$ K, and Reynolds number $Re_\infty = 1 \times 10^4$. The Reynolds number is based on a reference length taken as $L_\infty = 1.0$ m. At the left boundary of the computational domain, inflow conditions are fixed to freestream conditions. The portion of the lower boundary ahead of the flat plate, which is about a quarter of the plate's length, is assumed to be an inviscid surface that is taken as slip boundary conditions. As for the flat plate portion that is placed at the bottom boundary, no-slip boundary conditions are selected. At the top boundary, characteristic boundary conditions are used.

Comparisons of velocity profiles are presented in the form of normalized velocity components $u/V\infty$ vs the normalized distance from the wall $\bar{\eta} = y\sqrt{Re_x}/x$. Figure 6 shows the computed velocity profiles of the BGK scheme compared against the Roe FDS scheme and the Steger–Warming FVS scheme, along with the Blasius solution at x location that corresponds to the local Reynolds number

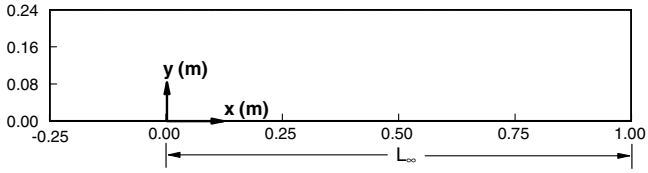

Fig. 5 Physical domain for the laminar flow over a flat plate.

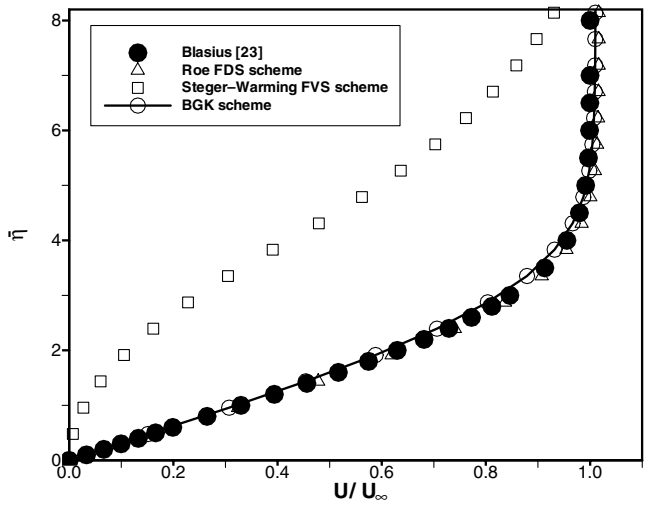

Fig. 6 Velocity profiles at $Re_x = 4000$ for the laminar flow over a flat plate.

of 4000. The circle symbol in black in this figure represents the exact solution of Blasius. As shown in the figure, an accurate boundary layer solution is obtained via the BGK scheme. The results by the Roe FDS are also in good agreement with the Blasius solution. Unfortunately, the Steger–Warming FVS scheme cannot resolve the boundary layer properly. As mentioned before, this is due to the high diffusion error in the scheme itself.

Comparisons of the computed skin friction coefficient C_f along the flat plate with the exact solution of Blasius are shown in Fig. 7. The Steger–Warming FVS scheme clearly shows that it significantly underestimates the friction coefficient as shown by Fig. 7. However, the BGK and Roe FDS schemes' results agree very well with the exact solution with Roe's result showing better quality.

C. Hypersonic Flow Passed 24 Degree Compression Ramp

To accurately predict the behavior of a hypersonic flow, the distributions of surface pressure and skin friction coefficients are required for assessing the accuracy of a numerical method. Hence, the experimental data quoted by Kim et al. [24] are used to validate the computed results of present numerical methods.

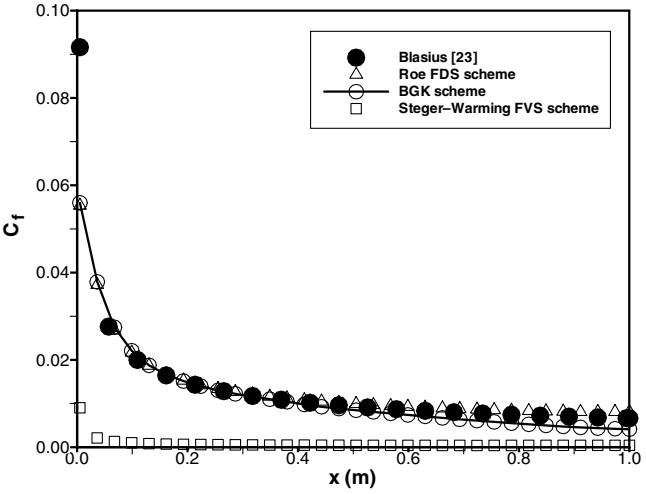

Fig. 7 Surface skin friction coefficients for the laminar flow over a flat plate.

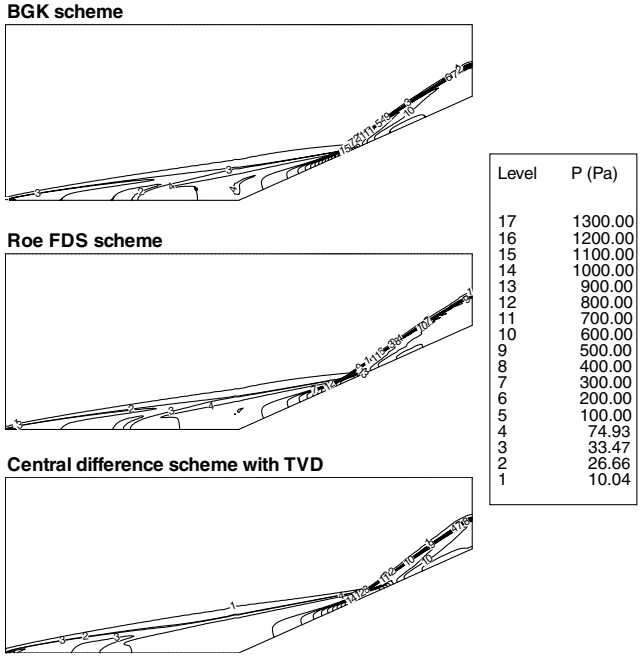

Fig. 8 Pressure contours for hypersonic flow passed a 24 deg ramp.

The freestream conditions used for this test case are as follows: Mach number $M_\infty = 14.1$, temperature $T_\infty = 72.2$ K, which is low enough to ensure real gas effects become unimportant, density $\rho_\infty = 4.84 \times 10^{-4}$ kg/m^3, pressure $p_\infty = 10.1$ Pa, absolute viscosity $\mu_\infty = 4.9369 \times 10^{-6}$ Pa · s, and Reynolds number $Re_\infty = 1.04 \times 10^5$. The reference length L_∞ is taken to be the length of the flat portion of the compression ramp.

As for the boundary conditions implemented for this flow problem, the following conditions are enforced: the lower boundary is assumed to be a nonslip condition with the isothermal wall maintained at $T_w = 297$ K, the left boundary is taken to be a supersonic inflow condition, the right boundary is assumed to be a supersonic outflow condition, and the top boundary is determined by a Riemann-type condition.

The first numerical results presented here would be the pressure contour plots for the BGK scheme, the Roe FDS scheme, and the central difference scheme with TVD formulation. These are depicted in Fig. 8. The computed flowfields indicate that a complicated shock–shock as well as shock–laminar boundary layer interactions are present. A leading edge shock wave intersects an induced shock wave, generated by the turning of the boundary layer near the junction to form a resultant shock accompanied by an expansion fan and contact surface, which influence the flowfield. Close examination of these contour plots shows that they are in good agreement with those found in [24], except the point of impingement of the shock for the central scheme is a bit displaced downstream of the ramp in comparison with the BGK and Roe schemes. This implies that the central scheme failed to predict the location of the shock accurately.

Second, the distribution of surface pressure coefficients is presented in Fig. 9. In this figure, the results from the BGK, Roe, and central schemes are compared with the experimental data. The C_p distributions produced by the BGK and Roe schemes follow closely the distribution of the experimental data, with the exception of the central scheme. The central scheme inaccurately predicts the location for the peak of the distribution in comparison with the BGK and Roe schemes. Upon close observation of the comparison made between the BGK and Roe schemes' distributions, one may discover that the BGK scheme is more precise in terms of predicting the location of the maximum value of C_p.

The final result presented here for this test problem would be the surface skin friction coefficient, which is shown in Fig. 10. In this figure, the skin friction coefficients for the BGK, Roe, and central schemes are compared with the experimental data. The C_f distribution generated by the BGK scheme is able to follow more

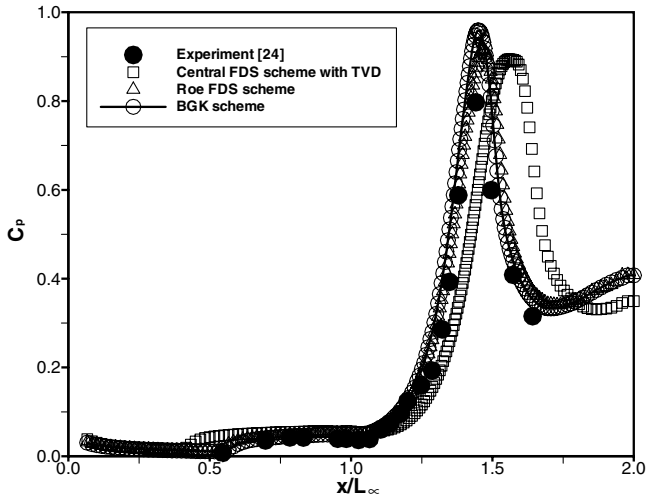

Fig. 9 Surface pressure coefficients for hypersonic flow passed a 24 deg ramp.

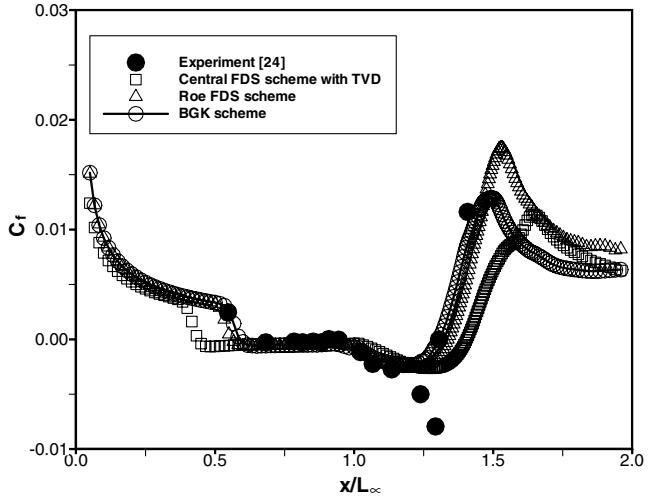

Fig. 10 Surface skin friction coefficients for hypersonic flow passed a 24 deg ramp.

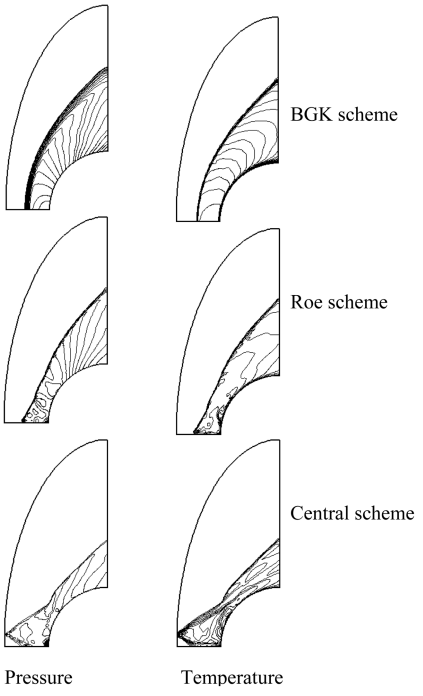

Fig. 11 Pressure and temperature contours for hypersonic flow around a blunt body.

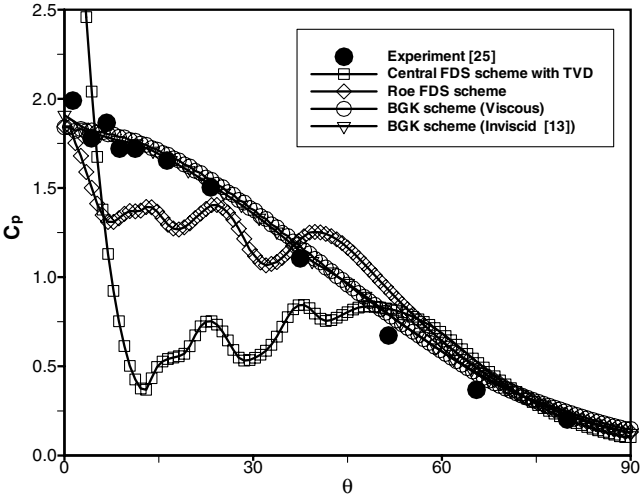

Fig. 12 Surface pressure coefficients for hypersonic flow around a blunt body.

accurately the distribution of the experimental data when compared with the results of the Roe and central schemes.

From all the comparisons shown in this part of the study, it can be observed that all the calculations agree very well with the experimental data, except for the central scheme, with the BGK scheme producing more accurate solutions compare to the Roe scheme.

D. Hypersonic Flow Around a Blunt Body

The last test problem undertaken in this study would be the steady hypersonic viscous flow around a quarter of a cylinder. This test case provides a very good opportunity to test the current flow solver for any possible failure because of the carbuncle phenomenon in a laminar viscous flow computation. Ong et al. [13] have undertaken a similar study to assess the computational capabilities of the BGK scheme but limited to inviscid flow calculations. To validate the results produced by the current numerical method, the experimental data from Lee [25] are used to make the necessary assessment.

The mesh used consists of 105×61 grid points with grids being clustered in the radial direction and uniformly distributed in the angular direction. The radius of the blunt body (i.e., inner body) is taken to be 0.0381 m. The minor and major radiuses of the outer body are assumed to be 0.75 times and 2.5 times the radius of the blunt body, respectively. The freestream conditions used to initialize the flow are as follows: Mach number $M_\infty = 15.622$, temperature $T_\infty = 45.17$ K, which is low enough to ensure real gas effects become unimportant, density $\rho_\infty = 1.814 \times 10^{-3}$ kg/m^3, pressure $p_\infty = 23.622$ Pa, absolute viscosity $\mu_\infty = 2.851 \times 10^{-6}$ Pa $\cdot$ s, and Reynolds number $Re_\infty = 5.11302 \times 10^4$. The Reynolds number is based on the freestream velocity and radius of the blunt body.

The conditions implemented for the boundaries of are as follows: the blunt body is assumed to have a nonslip condition with an isothermal wall maintained at $T_w = 300.33$ K, the top right boundary is to be a supersonic outflow condition, the outer boundary is fixed to the freestream condition, and the symmetry condition is applied at the lower boundary.

The contour plots for the pressure and temperature are presented in Fig. 11 depicting the comparisons between the BGK scheme with the Roe FDS scheme and the central difference scheme with TVD formulation. Comparing the results from this figure shows that the BGK scheme is able to resolve the entire flowfield accurately in comparison to the Roe and central schemes. As can be seen from Fig. 11, the Roe and central schemes produced numerical solutions with the occurrence of the so-called carbuncle phenomenon that have been reported by many studies in the past [13,25,26]. This shock instability is characterized by the unsymmetrical flow behavior and the protuberance of the bow shock as shown in Fig. 11.

Comparisons of surface pressure coefficients calculated by the numerical schemes with the experimental data are shown in Fig. 12. As illustrated in this figure, the result produced by the BGK scheme agrees very well with the experimental data. Both the Roe and central schemes failed to calculate the surface pressure coefficients accurately, and the results produced are quite oscillatory. In the same figure, the C_p distribution produced by the BGK scheme for inviscid flow computation also agrees very well with the experimental data.

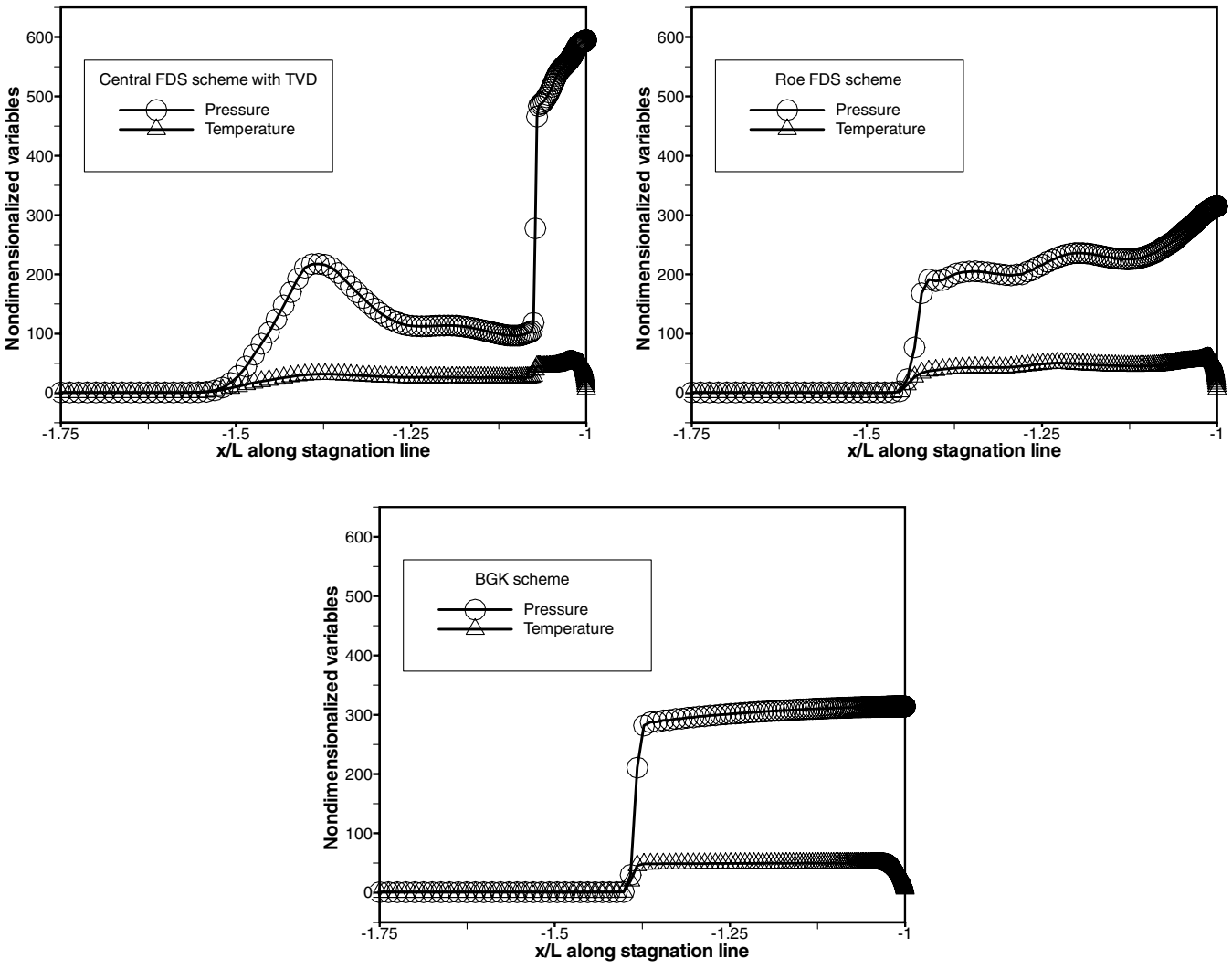

Fig. 13 Shock profiles along the stagnation line for hypersonic flow around a blunt body.

Last, the shock profiles along the stagnation line produced by the numerical schemes are examined. This is represented by Fig. 13, which compares the pressure and temperature profiles along the stagnation line among the three numerical schemes. As evident from this figure, the pressure and temperature profiles of the BGK scheme are able to maintain monotonicity across the shock. Such behavior of the flow has also been reported by Kim et al. [27], which presents their findings for a shock-stable Roe scheme. However, the Roe and central schemes lack this capability where the solutions of both schemes exhibit a serious oscillation after the shock.

The occurrence of shock instability in the Roe FDS scheme can be fixed if there was an entropy fix mechanism incorporated into the flow solver of this scheme. The reason for not implementing this improvement method into the Roe scheme in this paper is to enable the comparison of the numerical solutions obtained by each scheme during fundamental development. In other words, even without any additional remedy or improvement mechanism incorporated into the BGK scheme, it is still able to resolve the flow without experiencing the so-called carbuncle phenomenon for this test case. In addition, there have been various past published works that deal with this aspect of the Roe scheme such as reported in [26,27]. Thus, it would seem impractical to implement the entropy fix method to the Roe scheme for the current work.

V. Conclusions

A numerical flow solver based on the flux vector splitting concept of the BGK scheme has been successfully developed to simulate two-dimensional Navier–Stokes equations for laminar flow. Four test problems have been selected in this study to assess the numerical properties of this solver, namely, flow passed a 7.5 deg compression corner, laminar flow passed a flat plate, hypersonic flow passed a 24 deg compression ramp, and a hypersonic flow around a blunt body. The computed results for these flow problems clearly demonstrate that the BGK scheme is able to provide a very good resolution of the flow, which can be interpreted as an accurate flow solver. This claim is justified by the comparisons made between the numerical findings of the BGK scheme with existing experimental data and analytical solutions. Moreover, comparisons made between the BGK scheme's results with those from the upwind schemes further substantiate the notion that the BGK scheme is a robust and accurate numerical scheme.

Acknowledgment

The authors would like to acknowledge the support of the Ministry of Science, Technology, and Environment, Malaysia under the grant no. 09-02-08-10004-EAR.

References

[1] Roe, P. L., "Approximate Riemann Solvers, Parameter Vectors and Difference Schemes," *Journal of Computational Physics*, Vol. 43, No. 2, 1981, pp. 357–372. doi:10.1016/0021-9991(81)90128-5

[2] Chae, D. S., Kim, C. A., and Rho, O. H., "Development of an Improved Gas-Kinetic BGK Scheme for Inviscid and Viscous Flows," *Journal of Computational Physics*, Vol. 158, No. 1, 2000, pp. 1–27. doi:10.1006/jcph.1999.6400

[3] Peery, K. M., and Imlay, S. T., "Blunt-Body Flow Simulations," AIAA Paper 88-2904, 1988.

[4] Steger, J. L., and Warming, R. F., "Flux Vector Splitting of the Inviscid Gas Dynamics Equations with Application to Finite Difference Methods," *Journal of Computational Physics*, Vol. 40, No. 2, 1981, pp. 263–293. doi:10.1016/0021-9991(81)90210-2

[5] Van Leer, B., "Towards the Ultimate Conservation Difference Scheme V. A Second Order Sequel to Godunov's Method," *Journal of Computational Physics*, Vol. 32, No. 1, 1979, pp. 101–136. doi:10.1016/0021-9991(79)90145-1

[6] Hirsch, C., *The Numerical Computation of Internal and External Flows*, Wiley, New York, Vol. 2, 1990, Chap. 21.

[7] Xu, K., *Gas-Kinetic Scheme for Unsteady Compressible Flow Simulations*, Von Kármán Institute for Fluid Dynamics Lecture Series, Vol. 1998-03, Von Kármán Inst., Genese, Belgium, 1998.

[8] Ong, J. C., "Computational Analysis of Gas-Kinetic BGK Scheme for Inviscid Compressible Flow," M.S. Thesis, Univ. Putra Malaysia, Malaysia, 2004.

[9] Ong, J. C., Omar, A. A., Asrar, W., and Hamdan, M. M., "Development of Gas-Kinetic BGK Scheme for Two-Dimensional Compressible Inviscid Flows," AIAA Paper 2004-2708, 2004.

[10] Xu, K., "Gas-Kinetic Theory Based Flux Splitting Method for Ideal Magnetohydrodynamics," Institute for Computer Applications in Science and Engineering, NASA Langley Research Center, Report 98-53, Hampton, VA, Nov. 1998.

[11] Ong, J. C., Omar, A. A., and Asrar, W., "Evaluation of Gas-Kinetic Schemes for 1D Inviscid Compressible Flow Problem," *International Journal of Computational Engineering Science*, Vol. 4, No. 4, Dec. 2003, pp. 829–851. doi:10.1142/S1465876303002192

[12] Ong, J. C., Omar, A. A., Asrar, W., and Hamdan, M. M., "An Implicit Gas-Kinetic BGK Scheme for Two-Dimensional Compressible Inviscid Flows," *AIAA Journal*, Vol. 42, No. 7, 2004, pp. 1293–1301. doi:10.2514/1.2171

[13] Ong, J. C., Omar, A. A., Asrar, W., and Zaludin, Z. A., "Hypersonic Flow Simulation By The Gas-Kinetic BGK Scheme," *AIAA Journal*, Vol. 43, No. 7, 2005, pp. 1427–1433. doi:10.2514/1.11174

[14] Addusslam, S. N., Ong, J. C., Harun, M. M., Omar, A. A., and Asrar, W., "Application of Gas-Kinetic BGK Scheme for Solving 2-D Compressible Inviscid Flow Around Linear Turbine Cascade," *International Journal for Computational Methods in Engineering Science and Mechanics*, Vol. 7, No. 6, Nov. 2006, pp. 403–410. doi:10.1080/15502280600826357

[15] May, G., Srinivasan, B., and Jameson, A., "An Improved Gas-Kinetic BGK Finite-Volume Method for Three-Dimensional Transonic Flow," *Journal of Computational Physics*, Vol. 220, No. 2, 2007, pp. 856–878. doi:10.1016/j.jcp.2006.05.027

[16] Zhang, S. Q., Ghidaoui, M. S., Gray, W. G., and Li, N. Z., "A Kinetic Flux Vector Splitting Scheme for Shallow Water Flows," *Advances in Water Resources*, Vol. 26, No. 6, 2003, pp. 635–647. doi:10.1016/S0309-1708(03)00029-0

[17] Xu, K., Mao, M., and Tang, L., "A Multidimensional Gas-Kinetic BGK Scheme for Hypersonic Viscous Flow," *Journal of Computational Physics*, Vol. 203, No. 2, 2005, pp. 405–421. doi:10.1016/j.jcp.2004.09.001

[18] Ravichandran, K. S., "Higher Order KFVS Algorithms Using Compact Upwind Difference Operators," *Journal of Computational Physics*, Vol. 130, No. 2, 1997, pp. 161–173. doi:10.1006/jcph.1996.5561

[19] Hoffmann, K. A., and Chiang, S. T., *Computational Fluid Dynamics for Engineers*, Engineering Education System, Wichita, KS, Vol. 2, 1993, Chaps. 11 and 14.

[20] Jameson, A., Schmidt, W., and Turkel, E., "Numerical Solutions of the Euler Equations by Finite Volume Methods Using Runge–Kutta Time Stepping Schemes," AIAA Paper 81-1259, 1981.

[21] Niyogi, P., Chakrabartty, S. K., and Laha, M. K., *Introduction to Computational Fluid Dynamics*, Pearson Education, Upper Saddle River, NJ, 2005, Chap. 13.

[22] Simeonides, G., Haase, G., and Manna, M., "Experimental, Analytical and Computational Methods Applied to Hypersonic Compression Ramp Flows," *AIAA Journal*, Vol. 32, No. 2, 1994, pp. 301–310. doi:10.2514/3.11985

[23] White, F. M., *Fluid Mechanics*, McGraw–Hill, New York, 2005, Chap. 7.

[24] Kim, K. H., Lee, J. H., and Rho, O. H., "An Improved of AUSM Schemes by Introducing the Pressure-Based Weight Functions," *Computers and Fluids*, Vol. 27, 1998, pp. 311–346. doi:10.1016/S0045-7930(97)00069-8

[25] Lee, J. H., "Numerical Analysis of Hypersonic Shock-Shock Interaction Using AUSMPW+ Scheme and Gas Reaction Models," Ph.D. Dissertation, Department of Aerospace Engineering, Seoul National Univ., Seoul, Korea, 1999.

[26] Peery, K. M., and Imlay, S. T., "Blunt Body Flow Simulations," AIAA Paper 88-2904, July 1988.

[27] Kim, S. S., Kim, C., Rho, O. H., and Hong, S. K., "Cures for the Shock Instability: Development of a Shock-Stable Roe Scheme," *Journal of Computational Physics*, Vol. 185, No. 2, 2003, pp. 342–374. doi:10.1016/S0021-9991(02)00037-2

X. Zhong
Associate Editor